

Review

# A Comprehensive Review of Defects Genealogy in Olivines: From the Mineral World to Modern Electrode Materials

Eugene E. Nazarov <sup>1,\*</sup> , Dmitry A. Aksyonov <sup>1</sup>, Evgeny V. Antipov <sup>1,2</sup> and Stanislav S. Fedotov <sup>1,\*</sup>

<sup>1</sup> Center for Energy Science and Technology, Skolkovo Institute of Science and Technology, 3 Nobel Street, Moscow 121205, Russia; d.aksenov@skoltech.ru (D.A.A.); e.antipov@skoltech.ru (E.V.A.)

<sup>2</sup> Department of Chemistry, Lomonosov Moscow State University, Moscow 119991, Russia

\* Correspondence: eugene.nazarov@skoltech.ru (E.E.N.); s.fedotov@skoltech.ru (S.S.F.)

**Abstract:** The “Learning from nature” strategy is currently going through a renaissance period in modern materials science. Valuable experience gained by observing existing natural materials—minerals—paves the way towards design and modification of prospective functional materials for energy storage, which typically inherit the peculiarities of the parental minerals. The faults and flaws of the crystal structure—its defects—play a crucial role in determining both mechanical and electrochemical properties of the electrode materials. In this review, we endeavored to rethink the defect chemistry in triphylite-type positive electrode materials for metal-ion batteries and reflected on it from the perspective of their mineral olivine counterparts, thus establishing important correlations between point defects in olivine minerals and related electrode materials, their origin and formation processes. This work is meant to review geoscience and materials science perceptions of defects in triphylite-type electrode materials for Li- and Na-ion batteries.

**Keywords:** olivine; triphylite; defects; minerals; Li-ion battery; Na-ion battery; cathodes



**Citation:** Nazarov, E.E.; Aksyonov, D.A.; Antipov, E.V.; Fedotov, S.S. A Comprehensive Review of Defects Genealogy in Olivines: From the Mineral World to Modern Electrode Materials. *Energies* **2023**, *16*, 5083. <https://doi.org/10.3390/en16135083>

Academic Editor: Prodig K. Das

Received: 30 May 2023

Revised: 19 June 2023

Accepted: 25 June 2023

Published: 30 June 2023



**Copyright:** © 2023 by the authors. Licensee MDPI, Basel, Switzerland. This article is an open access article distributed under the terms and conditions of the Creative Commons Attribution (CC BY) license (<https://creativecommons.org/licenses/by/4.0/>).

## 1. Introduction

An olive-green-colored silicate-type mineral with an approximate composition of  $(\text{Mg,Fe})_2\text{SiO}_4$  (“olivine”) has long been an object under scrupulous study by geoscientists. It is widely believed to be the most abundant mineral in the Earth’s upper mantle and plays a key role in controlling manifold petrogenetic processes and physical properties of the Earth [1–3]. The geochemical and thermobarometric information recorded from olivines presents a useful tool in studies of rock formation and the geodynamics of the lithospheric mantle, formation and exploration of magmatic ores and deep-formed minerals such as pyroxenes and garnets. Nowadays the plural “olivines” presents a generic term to name a group of minerals with the  $\text{M}_2\text{XO}_4$  ( $\text{M} = \text{Mg, Fe, Mn, Ni, Ca}$ ;  $\text{X} = \text{Si, P}$ ) general formula, which adopts the parental olivine-type structure.

The interest in this class of minerals from the broader scientific community was reignited in 1997 when a lithium iron phosphate,  $\text{LiFePO}_4$ , a phosphate-based representative of the triphylite family, also commonly known as mineral triphylite, was proposed as a “rocks-shaking” abundant and safe cathode material for Li-ion batteries (LIBs) [4]. In contrast to layered oxide ( $\text{LiMO}_2$ ) cathode materials for LIBs, triphylites benefit from high thermal, cycling and chemical stability due covalently bonded  $\text{PO}_4$  anionic groups but have lower theoretic capacity. Furthermore, the triphylite materials can operate within thousands of charge/discharge cycles with low capacity decay and exhibit high specific capacity at elevated current densities [5]. Compared to spinel cathodes ( $\text{LiM}_2\text{O}_4$ ) featuring an isotropic 3D  $\text{Li}^+$  diffusion mechanism due to the cubic crystal structure, high cycling stability at increased current densities and near-5V operational potential in the case of Ni- or Co-based spinels, the total energy density of triphylites remains close or higher [6].

However, natural triphylites cannot be directly used for the production of electrode materials for LIBs, not only because they contain admixture phases, inclusions and intrinsic de-

fects typical for minerals, but also due to the diffusion limitations in monocrystals. To fully realize their electrochemical performance as an electrode material, triphylite phosphates should be skillfully prepared in the form of a nano-dispersed powder with a preferential crystallographic orientation of particles, and then suitably coated with conductive materials to mitigate low ionic and electric conductivities, respectively [7–9]. In hunting for the ideal synthesis method of  $\text{LiFePO}_4$ , many options were considered and developed: solid-state, sol-gel, freeze-drying, supercritical, ion-exchange, co-precipitation, hydro(solvo)thermal, etc., which led to high-quality electrode materials [10–12]. The path from the idea to a viable material and its further commercial deployment has taken many years. Alongside these developments,  $\text{LiFePO}_4$  became one of the most studied electrode materials ever. At the same time, in Na-ion batteries, triphylite-type  $\text{NaFePO}_4$  has also captured a lot of attention as an environmentally friendly and cheap electrode material. However, the stabilization of  $\text{NaFePO}_4$  in a thermodynamically metastable triphylite phase, rather than the stable maricite one, turned out to be tricky and complex despite the existence of the mineral analogues natrophyllite ( $\text{NaMnPO}_4$ ) and karenwebberite ( $\text{Na(Fe,Mn)PO}_4$ ) [13]. Additionally, low  $\text{Na}^+$  diffusion coefficients in  $\text{NaFePO}_4$  and the high volume mismatch between sodiated and desodiated phases of 17% significantly limit the practical application of  $\text{NaFePO}_4$  in sodium-ion batteries (SIBs) [14]. The calculated  $\text{Na}^+$  diffusion coefficients were found in the range of  $10^{-19}$ – $10^{-16}$  [14,15].

Among the features drastically influencing the electrochemical performance of  $\text{LiFePO}_4$  and related electrode materials are multiple types of defects, many of which were literally “reinvestigated” in synthetically made  $\text{LiFePO}_4$  despite being intrinsic and known for olivine-type minerals for decades. The ensuing rediscovery of the defects in  $\text{LiFePO}_4$  and its counterparts was presumably due to the low-level collaboration and loose interaction between physicists/chemists, who first introduced  $\text{LiFePO}_4$ -based electrodes and carried out the synthesis, and geologists/crystallographers, who had dealt with the natural olivine minerals for decades but mostly investigated petrogenetic properties and structural aspects. On the contrary, several types of defects, which are well-established in olivine minerals, have not been found so far in their synthetic counterparts. For instance, OH defects in the anion sublattice of  $\text{LiFePO}_4$  were first detected quite recently [16,17] despite being extremely common in natural olivines.

In this paper, we review the defects in natural and synthetic olivines (triphylites) and draw parallels between them with a focus on the physical properties guided by the introduction/elimination of various defects. Additionally, the influence of synthesis routes and the production parameters on the defect chemistry of olivines are elucidated. This work is intended to bridge the gap between geological and chemical interpretation of defect chemistry in olivine minerals and strengthen dialogue between geoscience and materials science communities.

## 2. Crystal Structure, Stability and Variety of Olivine-Type Minerals

In the most general view, olivines and isostructural compounds can be described with the  $\text{M}_2\text{XO}_4$  stoichiometry, where M is *s*, *p* or *d* metal or vacancy, and X is Al, Si or P. For minerals, this description is not exhaustive, because natural olivines normally feature different minor substitutions for M and X with other elements. A family portrait of the olivine minerals is schematically painted in Figure 1. Besides the end-members, olivines form a variety of solid solutions resulting in the plural minerals existing in nature.

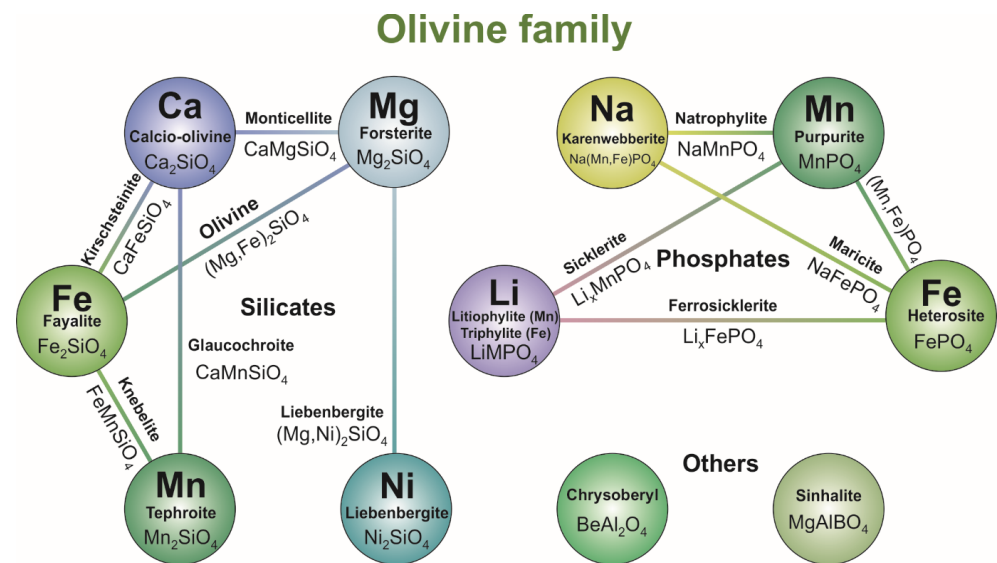


**Figure 1.** Schematic representation of the olivine mineral group.

The olivine crystal type is typically described within the orthorhombic symmetry, space group  $Pnma$  (#62) or its permutations such as  $Pmnb$ ,  $Pbnm$ , etc. (further on, all the considerations will rely on the  $Pnma$  setting for the sake of uniformity). The structure consists of individual  $\text{XO}_4$  tetrahedra (T site) corner- and edge-linked by octahedrally coordinated cations (M sites), as shown in Figure 2 [18]. The M-site cations reside in two independent positions, M1 and M2, whose environment usually deviates from the ideal octahedral symmetry. Since one O atom in the *hcp* lattice (Figure 3) produces one octahedral and two tetrahedral voids,  $\text{M}_2\text{XO}_4$  would contain eight tetrahedral and four octahedral voids for a formula unit. In other words, the olivine structure can be described as a slightly distorted hexagonal close-packed (*hcp*) array of O atoms, with 1/2 of octahedral voids being occupied by M and 1/8 of tetrahedral ones by X [19]. After applying the orthorhombic  $Pnma$  symmetry, two oxygen atoms are located on a mirror plane (4c position); the other two end up in the general (8d) position and degenerate. Simultaneously, due to the symmetry restrictions, eight tetrahedral voids transform into six non-equivalent voids, and four octahedral ones merge into two in  $\text{M}_2\text{XO}_4$ . Thus, metal atoms M split into the 4a and 4c M sites, and X occupies the 4c T position on the mirror plane, with other T positions remaining vacant. The M sites can also appear vacant. A more detailed representation in terms of Wyckoff positions and atomic coordinates is represented in Table 1.

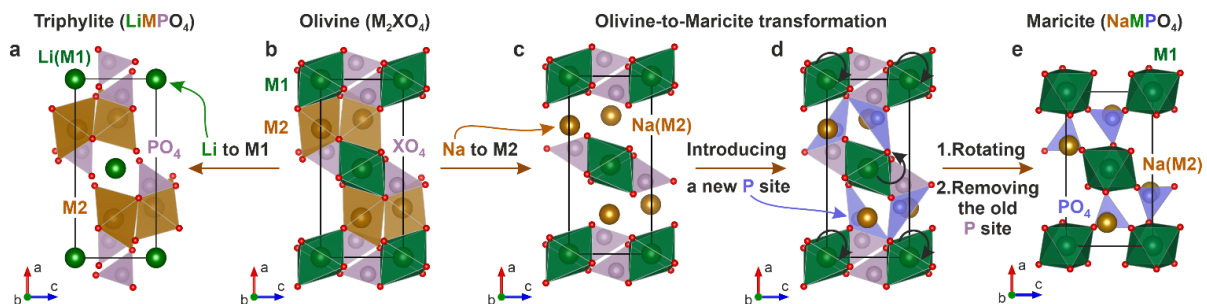


**Figure 2.** Polyhedral representation of the olivine-type structures (a,b) and their conversion to the maricite type (c–e) through the introduction of Na to the M2 site (c) and the shift of the P position (d). Red spheres designate oxygen atoms, a, b, c are the unit cell directions.

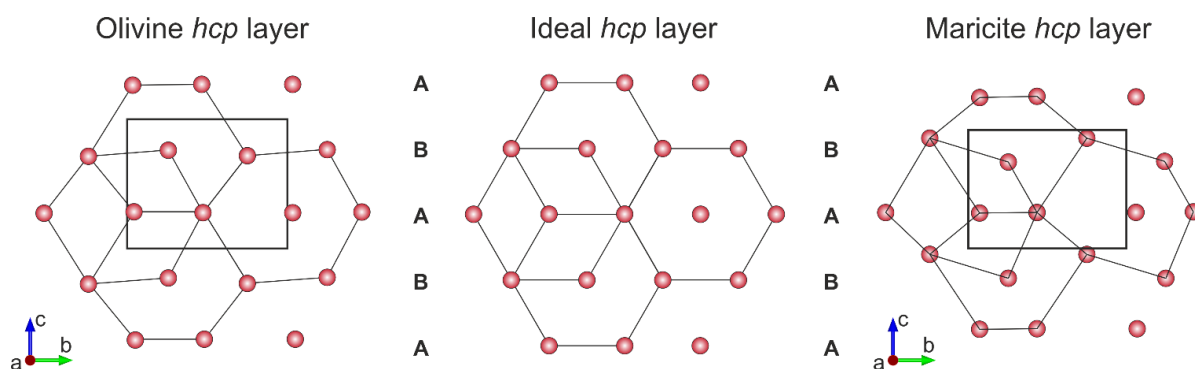


**Figure 3.** Arrangements and displacements of oxygen atoms in olivine (as in  $\text{MgFeSiO}_4$ ), maricite (as in  $\text{NaFePO}_4$ ) and ideal *hcp* layers; the black rectangle represents the unit cell, *a*, *b*, *c* designate the unit cell directions, A and B–*hcp* layers.

**Table 1.** Wyckoff positions and atomic coordinates of olivine, triphylite and maricite.

Structure Type		Atomic Coordinates *			
		Olivine ( $\text{M}_2\text{XO}_4$ ) [20]	Triphylite ( $\text{LiMPO}_4$ ) [7]	Maricite ( $\text{NaMPO}_4$ ) [21]	
Wyckoff Position	M1	$4a$	0, 0, 0	0, 0, 0	0, 0, 0
	M2	$4c$	0.28, $\frac{1}{4}$ , 0.98	0.28, $\frac{1}{4}$ , 0.97	0.34, $\frac{1}{4}$ , 0.97
	T	$4c$	<b>0.10, <math>\frac{1}{4}</math>, 0.40</b>	<b>0.09, <math>\frac{1}{4}</math>, 0.41</b>	<b>0.32, <math>\frac{1}{4}</math>, 0.04</b>
	O1	$4c$	0.08, $\frac{1}{4}$ , 0.75	0.09, $\frac{1}{4}$ , 0.73	0.12, $\frac{1}{4}$ , 0.75
	O2	$4c$	0.42, $\frac{1}{4}$ , 0.25	0.45, $\frac{1}{4}$ , 0.21	0.34, $\frac{1}{4}$ , 0.45
	O3	$8d$	0.17, 0.01, 0.25	0.16, 0.05, 0.28	0.12, 0.06, 0.32

\* Rounded to two digits after comma;  $\frac{1}{4}$  and 0 are coordinates for the *m*-plane positions in the cell.

Beside silicate-based representatives, there is a variety of non-silicate minerals adopting the olivine-type structure, including chrysoberyl ( $\text{BeAl}_2\text{O}_4$ ), sinhalite ( $\text{MgAlBO}_4$ ), lithiophilite ( $\text{LiMnPO}_4$ ), triphylite ( $\text{LiFePO}_4$ ), natrophylite ( $\text{NaMnPO}_4$ ), etc., which provide additional insights into the behavior of this structure type. Minerals of the triphylite–lithiophilite series,  $\text{Li}(\text{Mn,Fe})\text{PO}_4$ , occur in evolved granitic pegmatites that are enriched by both Li and P. The Li-rich pegmatites originate from the anatexis of Li-bearing metasediments or from very extensive differentiation of granitic magma. The deposition from gasses emanating from the crystallizing magma was also hypothesized [22]. Iron–manganese phosphates with the triphylite-type structure are common accessory mineral phases in pegmatites and some granites, particularly in the beryl–columbite–phosphate pegmatite subtype [23]. They also occur in some hydrothermal quartz-rich dikes. Triphylite–lithiophilite, sicklerite–ferrisicklerite and purpurite–heterosite [24] (Figure 1), all with a similar structure, are three important pegmatite solid solution series. The crystal structures of the phosphate minerals have similar features with those of olivines: the octahedral M1 site is mainly occupied by Li ions in triphylite–lithiophilite, partly occupied in sicklerite–ferrisicklerite or empty in purpurite–heterosite (Figure 2a). The paragenetic relationships in the structure of phosphate minerals are quite complex despite the simple chemical formulation: the  $\text{M}^{2+}$  metal in the M2 site in the solid solution series of triphylite–lithiophilite can undergo oxidation to  $\text{M}^{3+}$ , simultaneously leaching out Li to maintain the charge balance and triggering the phase transition to (ferri)sicklerite and further to heterosite. Since the minerals originate from hydrothermal dikes and granitic magma, the main production process for the triphylite-family materials is (solvo)hydrothermal treatment. This process allows both the production of monocrystals for precise structure refinement and the study of the defect chemistry and “ready-to-use” powders of cathode materials with a decent level of operational properties. The minerals’ origin helps in understanding the proper synthesis conditions for the production of materials with desirable properties.

A group of maricite minerals, phosphates with the  $\text{NaMPO}_4$  ( $M = \text{Mn, Fe, Zn, Mg}$ ) formula, is considered closely related to the olivine structure [25,26]. It also contains a highly distorted *hcp* array of oxygen atoms (Figure 3, right) with the inverse occupation of M1 and M2 positions and different positioning of phosphate anions in comparison to triphylites: Na, with a larger ionic radius, accommodates the bigger M2 site, inducing its distortion (Figure 2d,e), while the other metals reside in the normal octahedral M1 site (Figure 2c). It should be noted that mechanical switching of the M1/M2 positions for alkali and d metals in the olivine framework does not result in a maricite structure as it is usually alleged [27,28]; in order to accomplish the olivine-into-maricite transition, the phosphorus atoms have to be displaced to the adjacent (having a common basal plane) position (Figure 2) with a shift along the *a* and *c* axes (Table 1, in bold). In maricite, the phosphorus–oxygen tetrahedron has no shared edges with the M1 site octahedra, while in triphylite, the  $\text{PO}_4$  tetrahedra possess a common edge with the environments of both M1 and M2 sites. This maricite-type T site in the parent olivine structure is severely distorted (Figure 2d). A cooperative rotation of the octahedra chains with a simultaneous contraction of the unit cell along the *b* axis returns this T site to a normal tetrahedral shape, as shown in Figure 2e. Without the phosphate unit displacement, a new theoretical structural type with a quasi-layered structure can be obtained from the olivine (Figure 2c). The oxygen lattice in maricite also experiences significant distortion in comparison to the olivine/triphylite one (Figure 3, right). Some representatives, such as the minerals natrophyllite ( $\text{NaMnPO}_4$ ) or karenwebberite ( $\text{Na}(\text{Mn,Fe})\text{PO}_4$ ) [13], might preserve the triphylite-type or mixed occupation of the metal sites, while phosphorus resides exclusively in the olivine-type T site. At the same time, synthetic analogues of  $\text{Na}(\text{Mn,Fe})\text{PO}_4$  preferentially crystallize in the maricite structure [26], though sophisticated synthesis approaches were devised to stabilize the triphylite-type framework [29,30].

Taking into account the rich crystal chemistry and the variety of minerals in the olivine family, the understanding of possible crystal structure imperfections and their influence on the operational properties is a necessary aspect for designing new functional materials. A great example is triphylite-type cathode materials, which crystallize in the same structure type. Adopting structure features described for olivine and triphylite minerals for the technology of artificial cathode materials could lead to more efficient experimental designs in the field and production of the materials with desirable properties suitable for specific applications. In the following sections, the influence of point defects in cationic and anionic sublattices of triphylite cathode materials will be discussed, along with the strong connection to their silicate relatives. Additionally, a defect modeling will be outlined using density functional theory (DFT) calculations as a valuable tool for the prediction and description of the defect influence on the kinetics and diffusion properties of electrode materials.

### 3. Point Defects in Cationic Sublattice: The Influence on Transport and Electrochemical Properties of Triphylite Cathodes

#### 3.1. General Overview of Point Defects

From a chemical point of view, natural minerals are often complex systems, which indisputably have point or 0D defects (vacancies, interstitials, etc.), the presence of which is thermodynamically profitable, resulting in gaining entropy and reducing free energy. Their defects' structures might hold several types of defects simultaneously, which influence each other and determine manifold properties of the minerals, or comprise preferentially a single sort of defect. This section is intended to compare the intrinsic 0D defects in natural olivine-group minerals (mostly  $(\text{Mg,Fe})_2\text{SiO}_4$  and  $\text{Li}_x\text{FePO}_4$ ) with defects found in synthetic triphylite-type electrode materials (mostly  $\text{LiFePO}_4$ ) and draw parallels between their origin and impact on properties.

Point defects can drastically affect physical properties, such as color [31–34] and thermal [35,36], electrical [2,37,38] and ionic [39,40] conductivities, corresponding to the special defect types—vacancies, interstitials or impurities. Point defects can be subcategorized into several types. A vacancy defect means the absence of an atom in the crystal. It is

designated as  $V_M$ , where M is the name of an atom sublattice, where the atom moves out. A formal charge of the vacancy is equal to that of the M ion with an opposite sign. Another type of point defects—an interstitial—appears when an atom is displaced from its original site to a normally unoccupied free position in the lattice. Interstitials are expressed as  $M_I$ , and they have a formal charge equal to that of the M of the same sign. All intrinsic defects related to vacancy formation fall into two groups: Schottky and Frenkel defects. In the case of Schottky defects, a pair of anion and cation vacancies is formed and the total number of atoms per unit cell decreases. A Frenkel defect is realized when a vacancy and an interstitial defect attract each other and couple. In both cases, the crystal remains electrically neutral. It should be noted that Frenkel defect concentration is low in most cases, and such defects are strictly stoichiometric in contrast to Schottky defects, where the crystal can be off-stoichiometric. According to theoretical calculation, a Frenkel defect pair containing an M2 vacancy ( $V_{M2}''$ ) and Mg in the interstitial site ( $Mg_i^+$ ) is the most energetically favorable among other vacancy formations such as ( $V_{Si}''$ ) or ( $V_O$ ) [41].

Besides vacancies and self-interstitials, so-called substitutional defects such as impurity ions and antisite defects also exist in natural minerals, leading to physical and mechanical properties changes. Due to the relative flexibility of the olivine structure, substitutionals normally form solid solutions and can be isovalent or aliovalent. In the latter case, additional vacancies or charged species such as electrons or holes have to be present concomitantly to maintain electroneutrality. Here and below in the description of defects and their reactions, F.A. Kröger and H.I. Vink (i.e., Kröger–Vink) notations are used [42]; the list of all used notations are presented in Appendix A.

### 3.2. Defects of Cationic and Anionic Sublattice in Olivine Minerals

Olivines are particularly useful for the technological, geological and basic scientific studies of cation interdiffusion for enhancing the understanding of geological and planetary processes, such as volcano eruption and accompanying processes of magma flows and crystallization, and tectono-metamorphic events as well as physical and chemical features of the Earth's mantle, chemical heterogeneities, etc. [43]. Due to this, there has been a substantial number of experimental and theoretical studies of cation interdiffusion in olivine minerals of various compositions. Among them, Fe–Mg interdiffusion is the most common and most studied.

To consider defects such as antisites and the “off-stoichiometry” ones, it is more convenient to represent the crystal structure of olivines as the hexagonal close-packed counterpart of the cubic spinel structure  $A^{(tet)}B^{(oct)}_2O_4$ , i.e.,  $M^{(oct)}_2X^{(tet)}O_4$ . The  $M1O_6$  octahedra approaching a trigonal antiprism are centrosymmetric. The  $M2O_6$  octahedra are more distorted and have two O atoms of one  $XO_4$  tetrahedron each. In some *d* metals containing mixed olivines, such as  $(Fe_xMg_{1-x})_2SiO_4$ ,  $(Co_xMg_{1-x})_2SiO_4$  and  $(Ni_xMg_{1-x})_2SiO_4$ , the divalent cations occupy crystal structure positions according to their ionic radius and crystal field stabilization energy as well as M–O bonding nature [44]. Thus, the cations might form antisite defects in the M1 and M2 positions (there are also other terms such as interdiffusion or interexchange), for example, in  $(Mg_{1-x}Fe_x)[Fe_{1-x}Mg_x]SiO_4$ .

The first detailed study of the Fe–Mg interdiffusion in olivines was presented in [45], where compositional dependence and clear diffusion anisotropy was revealed with higher diffusion coefficients along the *b* axis. Later, other authors carried out Fe–Mg interdiffusion experiments at various pressures (from 3 GPa to 9–12 GPa) and temperature ranges (873–1673 K) [43,46–48]. Fe–Mg interdiffusion coefficients in olivines were measured at atmospheric pressure taking into account the Fe:Mg ratio, temperature, crystal orientation and oxygen fugacity using thin films. The obtained results demonstrate a strong correlation with the Fe fraction but are weakly linked to oxygen pressure. A quantitative model describing Fe–Mg interdiffusion coefficients in olivine for modeling the above-mentioned natural process was developed considering the point defects presenting in the crystal structure [49]. The results obtained in [49] confirm the findings obtained in [50], which showed a negligible correlation with oxygen fugacity and no significant impact on composition

variation. From numerous calculations of Fe–Mg interdiffusion coefficients ( $D_{\text{Fe–Mg}}$ ) in olivine, it was found that cation vacancies strongly depend on the concentration of ferric iron ( $\text{Fe}^{3+}$ ) formed at elevated temperatures and increased oxygen fugacity values. Thus, the Fe–Mg interdiffusion in olivine occurs by the vacancy mechanism, which could be described as cation position exchange with a nearby vacancy. The suggested diffusion mechanism is a function of temperature, pressure and oxygen fugacity, but at the same time, it is independent of the concentration of any impurities in the crystal structure [51].

The site preference of Fe in  $\text{FeMgSiO}_4$  was investigated in [52] by means of density functional theory calculations. It was found that at equilibrium conditions ( $T = 0$  K), iron ions occupy the M2 site due to the higher Fe2–O bond covalence compared to Fe1–O. The connection pattern of  $\text{FeO}_6$  octahedra at M2 results in the chain formation by sharing the corner oxygen atoms. The obtained connection pattern makes the structure more stable compared to a less connected network by sharing the edge oxygen atoms in the case of M1 site occupation.

For the characterization of Fe–Mg intermixing, a distribution coefficient  $K_D$  is applied, reflecting the atomic fraction of Fe and Mg at the M1 and M2 sites. The coefficient is represented by the following formula [53]:

$$K_D = \frac{[\text{Fe}_{\text{M2}} \cdot \text{Mg}_{\text{M1}}]}{[\text{Fe}_{\text{M1}} \cdot \text{Mg}_{\text{M2}}]}$$

$K_D$  is  $> 1$  in the case of perfectly ordered and close to 1 for a completely disordered material. A number of experimental techniques were applied for the investigation of cation sublattice disorder and its influence on materials properties: powder and single crystal diffraction techniques including synchrotron and neutron diffraction, spectroscopy [54] and microscopy experiments. The main parameters influencing the defect structure of olivine minerals are temperature, Fe/Mg ratio, oxygen fugacity and pressure. The neutron diffraction experiment conducted in [53] at room temperature confirms the above-discussed DFT calculations reported in [52], where a stoichiometric material was considered. In increasing the temperature, the site preferences for Fe were reversed, reaching the so-called cross-over temperature, above which the Fe ions start occupying the M1 site indicating the presence of antisite defects in the crystal structure [53]. The reason for the observed crystallographic site changing is the difference between bond-length thermal expansions of Mg–O and Fe–O bonds; the higher covalency of the Fe–O bond is responsible for the lower thermal expansion. The  $\text{M1O}_6$  and  $\text{M2O}_6$  octahedra volume was measured before and after reaching the “cross-over temperature”; it was stated that the  $\text{M2O}_6$  volume is larger at lower temperature but increases the volume as the temperature rises, while the opposite is observed for the M1 site, indicating the transition of more covalently bonded Fe–O into the M1 site [53]. Close results were obtained in [50], where in situ Mössbauer spectroscopy was applied for the detection of the M1 and M2 disorder. When the temperature increases up to 800 °C, the Fe occupancy of the M1 site approaches 60%, such that following the exponential fit suggested by the authors, it is possible to achieve a completely disordered material at a temperature of ~300 °C [53].

The influence of antisite defects in olivines on mechanical and dielectric properties is described in [55]. DFT calculations were used to evaluate the effect of the cation disorder on elastic properties of olivines [55]. It was stated that the presence of iron at the M1 site results in the deformation of the crystal lattice along the  $b$  axis and the stiffness reduction along the  $a$  and  $b$  axes with a slight hardening in the  $c$  direction [55], making the material more vulnerable to mechanical deformation. The graphical representation of the elastic modulus dependence on the cation disorder is represented in Figure 4a. The incorporation of Fe at the M1 site results in a decrease in the  $G_{13}$  component of the elastic modulus in the whole range of the experimental pressure, while for  $G_{12}$  and  $G_{23}$ , the difference is not that significant [55].

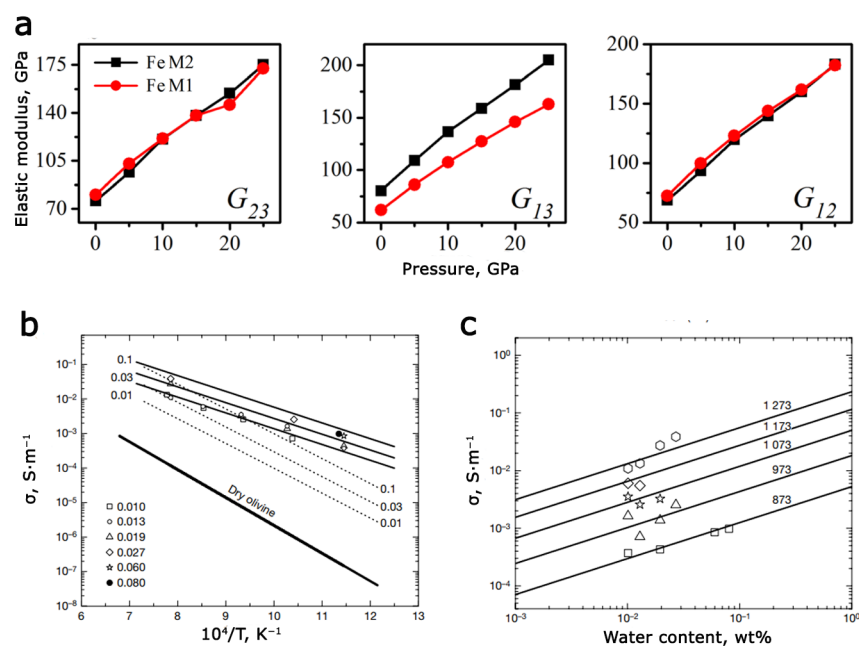


**Figure 4.** The influence of defects on properties of olivine silicates: (a) the effect of antisites on mechanical properties of  $\text{MgFeSiO}_4$  [55], (b) the temperature dependence of electronic conductivity (the numbers represent the water content in  $\text{MgFeSiO}_4$ ), and (c) the impact of hydroxyl defect concentration on electronic conductivity of hydrogen-bearing olivine at different temperatures (the numbers represent the experimental temperature, each symbol designates the data at a given temperature above the solid line) [2].

The cation disorder plays a crucial role for distorting the crystal structure of the material and thus influencing the key properties of minerals. At the same time, the formation mechanism as well as the dependence of mineral genesis conditions on the defect concentration opens up new insights for functional materials design. The consideration of the differences and similarities between natural olivine minerals and artificial triphylite cathodes helps in adjusting the synthesis processes for production of less defective materials. Since antisite defects for both classes influence the diffusion and mechanical properties in a very similar way, one might consider natural minerals as a guide for tuning the materials properties and use the natural formation conditions as starting points for functional materials synthesis.

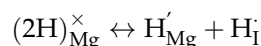
The anionic sublattice of olivine silicates could be in turn represented as a discontinuous arrangement of  $\text{SiO}_4$  tetrahedra. As the silicate's formation is closely related to the hydrothermal conditions, the presence of water strongly affects the defect chemistry of the materials.  $\text{H}^+$  and  $\text{OH}^-$  species formed during water dissociation incorporate into vacant and/or interstitial lattice sites [56]. Three possible reaction pathways are associated with water inclusion in olivine silicates: incorporation into metal or silicon vacancies and partial metal oxidation for the preservation of charge balance [57].

The first scheme includes the protonation of metal vacancy at the M1 site. The most stable configuration is observed when H atoms are bonded with O2 atoms of the neighboring silicate tetrahedra [58]. The presence of defects can be detected by FTIR, revealing the vibration modes of OH groups. The two modes occurring at  $3225\text{ cm}^{-1}$  and  $3212\text{ cm}^{-1}$  are assigned to the out-of-phase and in-phase stretching of the OH groups, respectively [58]. Using ab initio calculations, the most stable structural model for the M2 vacancy mechanism involves two hydrogen atoms bonding with the O3 atoms [59]. Considering the possibility of hydrogen incorporation into the M1 site, the total energy of the structural model was found to be 0.593 eV larger compared to the defect inclusion into the M2 site. Thus, the substitution at the M2 crystallographic site seems more preferable. The structure changes associated with the incorporation of defects into the crystal structure could result

in lowering the symmetry of the unit cell from  $Pnma$  down to monoclinic  $P2_1/m$  or  $P2_1$  or even triclinic  $P1$ , with higher stability of the monoclinic unit cell [59].

The  $\text{Fe}^{2+}$  oxidation in the olivine crystal structure is attributed to the shift from the uniform ion distribution between the M1 and M2 sites to the predominant M1 occupation by  $\text{Fe}^{3+}$  due to the lower ionic radius. In this case, the protonation of either O1 or O2 oxygens takes place. The detection of the specific configuration is possible by IR spectroscopy with a theoretical signal at a wavenumber of  $3388\text{ cm}^{-1}$  and  $3245\text{ cm}^{-1}$  for O1 and O2, respectively. The third possible scenario concerns the presence of a ferric ion at the M2 site with an H atom bonded to the O3 oxygen, manifesting a characteristic band at  $3374\text{ cm}^{-1}$ . The described model suggests the combination of the three described scenarios in natural materials in the mantle at elevated temperatures with the relative fraction of 30–40% [60]. Another scenario is close to the “titanoclinohumite defect” observed in titanium-rich garnets [61]. Like in the case of titanium, the ferric ion and  $\text{H}^+$  compensate a partially protonated Si vacancy, which could be represented by the following Kröger–Vink notation:  $[\text{Fe}'_{\text{M1}}(3\text{H}'_{\text{Si}})]^\times$ . Consequently,  $\text{Fe}^{3+}$  occupies the M2 site and shares the edge with a vacant silicon site. The presence of this complex defect could be traced by the appearance of the three IR bands in the region of  $3250\text{--}3540\text{ cm}^{-1}$  (57).

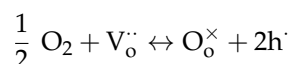
The presence of hydrogen-associated defects in olivines significantly affects the conductivity of the material, since the protons occupying the Si vacancies could serve as additional charge carriers along with the electron holes created by the ferric ions' incorporation at the M2 crystallographic site. The water-content-dependent conductivity is best explained by the motion of free protons [2,62,63]. In one interpretation, two protons present at the M1 site can split up and form an interstitial proton:



Indeed, the conductivity is normally determined as a sum of electron hole conductivities from  $\text{Fe}^{3+}$  substitution at the M1 site, the proton conductivity and holes constitute:

$$\sigma = \sigma_{\text{Fe}} + \sigma_{\text{H}} + \sigma_{\text{h}}$$

Therefore, the conduction mechanism differs between wet and dry samples [2]. For wet olivine samples, it should be mostly due to charged species, such as hydrogen ions ( $\sigma_{\text{H}}$ ). Then, for water-free olivine, the conduction mechanism is considered to be the migration of electron holes ( $\sigma_{\text{h}}$ ) formed by oxygen vacancies:



As the number of charge carriers increases, the electronic conductivity of water-incorporated olivines rises (Figure 4b,c).

Overall, defect incorporation in olivines brings drastic changes in the structure and mechanical and electric properties of the minerals, as validated by numerous examples above which emphasize the role of defect chemistry in designing the desired properties of artificial analogues. The graphical representation of the crystal structure defects on mechanical properties and electrical conductivity is represented in Figure 4.

### 3.3. Defects of Cationic and Anionic Sublattice in Synthetic and Natural Triphylites

The rich variety of crystal structure defects of olivine silicates could be translated to the triphylite minerals and synthetic cathodes due to the same structure type. The most important types of defects and their formation conditions are presented in Figure 5.

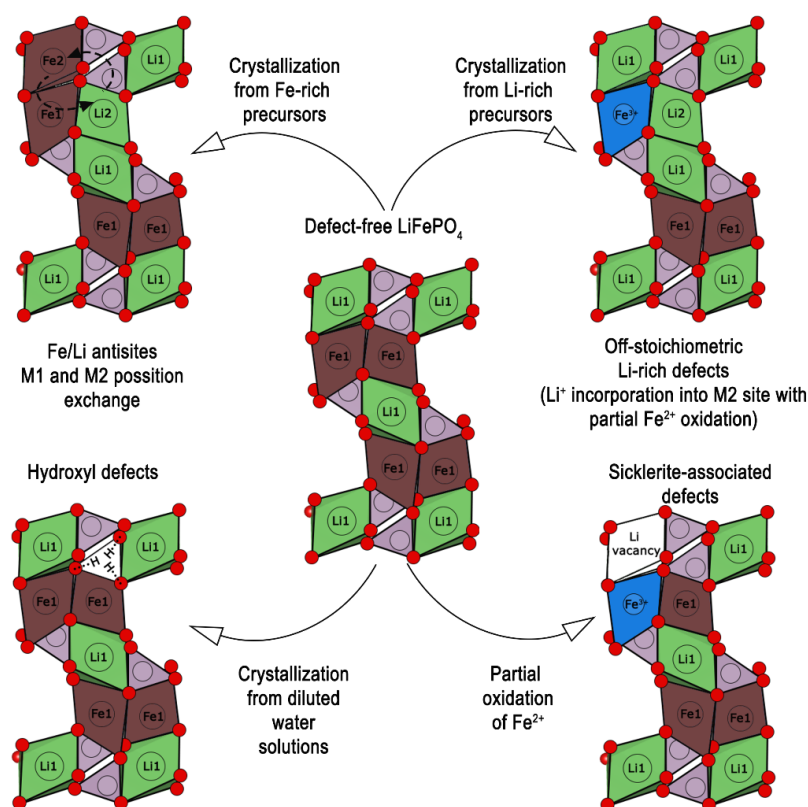


Figure 5. The main triphylite structure defect types.

The most well-studied defects for synthetic triphylites are antisites, since their presence drastically impacts the operational properties of the material, for example, on the  $\text{Li}^+$  diffusion coefficient, its de/intercalation mechanism and the specific capacity of the cathodes. An antisite defect could be described as an atomic arrangement when a position of a particular atom is occupied by a different chemical species contained in the crystal. Antisite defects are a feature of a number of ionic and covalent functional inorganic materials. In a crystal with the formula  $\text{AB}$ , the antisite defects are represented as the A atom positioned at the site normally occupied by the B atom, or vice versa. The formation of an antisite defect pair consisting of the B atom at the A atom site,  $\text{B}_\text{A}$ , and the A atom at the B site,  $\text{A}_\text{B}$ , can be described in terms of a quasi-chemical equation:  $\text{A}_\text{A} + \text{B}_\text{B} \rightarrow \text{A}_\text{B} + \text{B}_\text{A}$ . The formation of antisite defects usually occurs during crystal growth, when atoms are misplaced from their normal sites during the crystallization of a material. Alternatively, the defects can be promoted by applying the sufficient energy required for atom movement when the crystal is formed [64,65].

The importance of antisite defects is manifested in a number of lithium intercalated electrode materials, in which  $d$  metal and lithium cations of a close radius usually feature a well-ordered framework. The antisites drastically influence the kinetics and electrochemical performance of triphylite-type cathodes,  $\text{LiMPO}_4$ , since the lithium motion normally proceeds through one-dimensional (1D) channels (along the  $b$  axis) but not across the channels because of a high energy barrier. Unlike the two-dimensional  $\text{Li}^+$  diffusion occurring in layered metal oxides, the diffusion of Li ions in  $\text{LiMPO}_4$  can be easily blocked if there is a defect representing an obstacle in the channel. Thus, a fundamental problem in the triphylite-structured phosphates is the 1D nature of the  $\text{Li}^+$  pathways, which become effectively impassable due to the antisite defects, i.e.,  $\text{M}^{\text{n}+}$  cations occupying Li sites.

The antisite defects were found in natural triphylites by means of X-ray diffraction and Mössbauer spectroscopy experiments, where the total  $\text{Fe}^{2+}$  occupying the M1 site was determined as 8% [24]. Another study of natural triphylite suggests 4% of  $\text{Fe}^{2+}$  at the Li site and the presence of  $\text{Fe}^{3+}$  at the M2 site, with Li leaching from the M1 site forming a

vacancy [66]. The presence of ferric ions in natural triphylites could be explained by the partial oxidation of Fe or Mn and the transition to the sicklerite mineral [67]. Both ferric ions and sodium vacancies at the M1 site were found in the karenwebberite mineral [13]. Furthermore, the oxidation process is similar to the triphylites. The very close processes associated with the de/insertion of lithium ions from the cathode material undergone during battery operation [68] makes the study of the weathering process of triphylites minerals extremely important, especially from the point of view of defect formation. The close relation of the nature of the oxidation process and Li leaching from minerals and electrochemical  $\text{Li}^+$  de/intercalation could help us to understand the defect formation evolution and use natural processes as references due to their equilibrium.

The first systematic study of defects in synthetic  $\text{LiMPO}_4$  was performed by Islam et al., who applied interatomic-potential simulations. It was observed that the required energy for the antisite-pair defect formation  $\text{Li}_{\text{Fe}}$  and  $\text{Fe}_{\text{Li}}$  (Li atoms at the Fe site and Fe atoms at the Li site) in  $\text{LiFePO}_4$  was the lowest ( $E_{\text{antisite}} = 0.74$  eV), compared to Frenkel ( $V'_{\text{Li}} + \text{Li}_{\text{Li}}''$ ,  $V''_{\text{Fe}} + \text{Fe}_{\text{Fe}}'$ ) or Shottky defects [69,70]. Based on theoretical calculation, Malik et al. also came to similar results about the energetics of the defects: the formation energy of the  $\text{Fe}_{\text{Li}}' - \text{Li}_{\text{Fe}}''$  antisite pair lies in the range of 0.515–0.55 eV [71]. The formation energies of antisite defects were calculated for synthetic  $\text{NaFePO}_4$  in [72] by means of density functional theory calculations. Like for  $\text{LiFePO}_4$ , the antisites have the lowest energy of 0.86 eV compared to Na or Fe Frenkel-type defects (2.25 and 2.29 eV, correspondingly). An investigation of Na vacancy ordering was conducted in [73] using microscopic and diffraction techniques, where it was stated that the symmetry of  $\text{Na}_{0.7}\text{FePO}_4$  transforms into monoclinic ( $P2_1/a$  space group) with a regular pattern of Na vacancies and ferric ions compensating the charge balance. The same phase was detected during the operation of  $\text{NaFePO}_4$  with the reason of a lower volume mismatch between sodiated and desodiated phases [74]. The effect of particle size was also taken into account; the probability of the defect formation in nanosized particles was significantly lower, leaving most of the channel available for fast 1D diffusion of  $\text{Li}^+$  [75]. It was shown that the probability of the exchange of Li/M positions in the case of  $\text{LiFePO}_4$  increases with increasing concentration of  $\text{Fe}^{3+}$  ions [75,76]. The same results were observed in olivine silicates, where  $\text{Fe}^{3+}$  ions tend to occupy the M1 sites due to the lower ionic size, leading to the increase in the ion interexchange [60]. The most important conditions influencing defect concentration and distribution are synthesis scheme, temperature and particle size. Among all the suggested synthesis routes, the hydrothermal one is the closest to naturally formed  $\text{LiFePO}_4$ . However, this method might easily lead to a large concentration of Fe antisite defects in the obtained material [77]. According to the current understanding, the amount of Fe/Li antisite defects can be gradually reduced by long synthesis time (5–7 h) and elevated temperatures (180–200 °C) [78], by switching to non-aqueous solvents (ethylene glycol or ethanol) [79] or by a heat treatment at high temperatures ( $T > 600$  °C) [80]. However,  $\text{LiFePO}_4$  produced by a hydrothermal/solvothermal route at low temperatures (<175 °C) inevitably forms  $\text{Fe}_{\text{Li}}$  antisite defects [81]. Despite the unavoidable formation of antisite defects during material synthesis, there is a possibility of their elimination during the electrochemical annealing by inducing Li into the material's structure during discharge. In [82], Li/Fe antisites were annihilated by a partial electrochemical reduction of the defective material containing ferric ions. The reduction of ferric ions in the crystal structure during the discharge process lowers the activation energy of  $\text{Li}^+$  migration from the M2 site to the M1 site. Along with the Li intercalation into the crystal structure and the recombination of the defects, the total amount of antisites was decreased from 4% to 1.86%. Furthermore, studies showed that  $\text{Fe}_{\text{Li}}$  defects in  $\text{LiFePO}_4$  can be recombined while heat-treated above 500 °C [83]. Furthermore, single phase samples with 4% of Li:Fe antisites have been reported for the very low-temperature synthesis of nanoparticles based on a co-precipitation process [84]. The formation of nanopowders is principally important as nanosizing provides enhanced  $\text{Li}^+$  diffusion in  $\text{LiFePO}_4$  as well as a diminished amount of antisite defects. The concentration of antisite defects in a mechanochemically produced

LiFePO<sub>4</sub> was estimated to be as low as 3–4% [85,86]. In addition, considerable efforts have been made to decrease the diffusion pathway length of Li<sup>+</sup> ions via an oriented growth of LiFePO<sub>4</sub> particles along the *b* axis. Zhao et al. have produced (010)-oriented LiFePO<sub>4</sub> sheetlike particles with an average thickness of 50 nm [87]. The controlled orientation of the material particles promotes the fast diffusion of Li<sup>+</sup> ions as well as making it possible to minimize the amount of conductive additive for decent electrochemical performance of the material [88]. Paolella et al. [89] realized an inexpensive hydrothermal synthesis of LiFePO<sub>4</sub> nanoparticles and succeeded in minimizing the Fe–Li antisite defect concentration to 1% using calcium ions. The suggested mechanism includes the formation of an intermediate LiCa<sub>10</sub>(PO<sub>4</sub>)<sub>7</sub> composition followed by the formation of an LiCaPO<sub>4</sub> phase. The next step is a topochemical reaction leading to the production of LiFePO<sub>4</sub>. The remaining Ca ions occupy the M2 site, forcing Li<sub>Fe</sub> defects to segregate on the materials surface [89]. However, this method is too complex and the capacity at high current density is comparable with the conventional LiFePO<sub>4</sub> with 3–4% of antisites. Much recently, Zou Y. et al. developed a cost-effective method to suppress Fe–Li antisite defects to 0.23% using the “egg-box” structure in alginate and reduced graphene oxide [90]. The described approach makes it possible to create a uniform ion distribution of mixed Li–Fe–P alginate inside the graphene oxide layer due to the hydrogen bond formation between hydroxyl alginate groups and the surface hydroxyl layer of graphene oxide [90]. Therefore, the hydro/solvothermal synthesis might be successfully used to obtain an LiFePO<sub>4</sub> with a low antisite defect concentration. In addition, antisite defects could manifest during electrochemical cycling of the material: mechanical stress induced by Li<sup>+</sup> de/intercalation results in cation rearrangement, which leads to the local charge disbalance, although the process is almost reversible [91]. It should be noted that exchange defects were observed directly experimentally using various methods. The important studies of Chen J. et al. (via in situ X-ray diffraction) [83], K. Jensen M. et al. (via neutron powder diffraction) and Chung S.-Y. et al. (via HAADF-STEM) [92] stated that the Li<sub>Fe</sub> antisite defects are formed by Fe<sup>2+</sup> ions positioned in the M1 sites, thus blocking the Li<sup>+</sup> diffusion pathways. Different resolutions and sensitivities provided by the diffraction and microscopic experimental techniques resulted in the uncertainty of the exact contraction of the defects. For example, HAADF-STEM imaging concedes a variation of antisite defect concentration of up to 15%, while high-resolution neutron diffraction experiments on the same sample indicated that the total fraction of antisite defects is as low as 1% [93]. Seemingly, the variation could be deduced by the local aggregation of the defects, compared to the homogeneous distribution through the whole lattice [92]. Applying divalent Ca or Mg cations for decreasing antisite defects in synthetic triphylite phosphates proves to be a useful tool and could be considered as a natural hint for improving the key properties of the materials, since Mg and Ca frequently accompany the formation of triphylite minerals [94].

The effect of antisite defects on Li diffusion has been investigated extensively using ab initio calculations [71], empirical models and classical molecular dynamics simulations [95]. Direct dynamical simulations [91,96] suggested that antisite defects may enhance the interchannel crossing for Li migration, enabling a transition from quasi-1D to 2D diffusion. Thus, the interaction of exchange defects with each other [97] and cationic vacancies for LiFePO<sub>4</sub> and LiMnPO<sub>4</sub> was studied in detail. The higher site preferences for Mn in LiMnPO<sub>4</sub> was found compared to Fe in LiFePO<sub>4</sub> [97]: the total amount of antisite defects was found to be 2%, which is two times lower for analogous LiFePO<sub>4</sub>. Another distinct difference between the two triphylites is that for the Mn analogue, the aggregation of defects was not observed and the defects were randomly distributed in the crystal structure of the material, while for LiFePO<sub>4</sub>, a strong tendency of defects to coalescence is more energetically favorable [97]. The obtained results correlate well with the site preferences in Fe- and Mn(Co)-containing natural olivine silicates, where the presence of Mn or Co restrains the d metal transition to the M1 site [44,98].

It is worth mentioning the off-stoichiometric materials preparation resulting in the formation of so-called Li-rich triphylites, where additional Li ions occupy the M2 site with

the partial oxidation of  $\text{Fe}^{2+}$  remaining at its crystallographic position. First, the concept was introduced in [99], where a 5% excess of  $\text{LiFePO}_4$  cathode material was synthesized. Then it was established by means of DFT calculations that the presence of additional Li ions at the M2 site of  $\text{LiFePO}_4$  will result in increasing  $\text{Li}^+$  diffusion coefficients and a switch of the diffusion mechanism from conventional 1D to a two- or even three-dimensional one, depending on the Fe substitution fraction. The maximum amount of excess  $\text{Li}^+$  in triphylite was calculated as 12.5% [100]. Followed by the described approach, a number of successful experimental confirmations of Li-rich triphylite synthesis were published. The reported concentration of additional Li ions present in the crystal structure fell in the range of 5–10%, which is sufficient for enhancing the electrochemical performance at high C-rates and reducing the polarization at elevated current densities [7,9]. The comparison between stoichiometric and Li-rich  $\text{LiFePO}_4$  was performed in refs. [9,99]. Electrochemical performance of the conventional and Li-rich materials demonstrated in Figure 6a,c,d makes it possible to suggest the higher output specific capacity at elevated C-rate for Li-rich materials. At lower C-rates, conventional material exhibits slightly higher output capacity (Figure 6a,b) due to higher concentration of electrochemically active  $\text{Fe}^{2+}$ . For the detection of  $\text{Fe}_{\text{Li}}$  defects, a combination of diffraction, spectroscopic and microscopy techniques is applied. In a recent paper [7], this concept was transferred to a higher energy density  $\text{LiFe}_{0.5}\text{Mn}_{0.5}\text{PO}_4$  cathode material. Using joint neutron and synchrotron diffraction coupled with Mössbauer spectroscopy and EELS as well as HAADF-STEM, the excess  $\text{Li}^+$  in the crystal structure was estimated as 7%, revealing the beneficial impact on promoting the  $\text{Li}^+$  de/intercalation process to follow mostly a solid-solution mechanism. The electrochemical performance at high current densities was close to the reported values of the Li-rich  $\text{LiFePO}_4$ , rendering this approach a reliable tool for enhancing transport and electrochemical properties of triphylite-type cathodes [7].

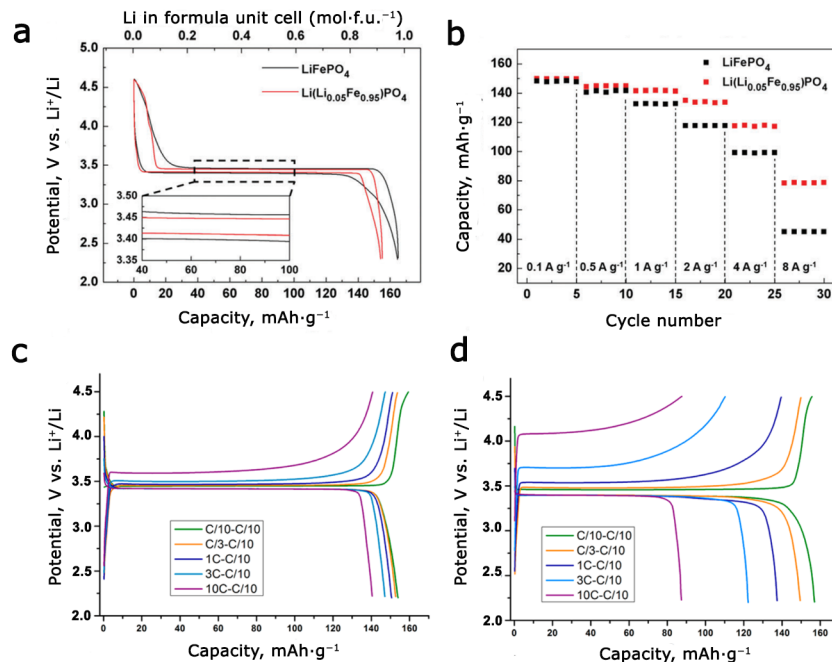


**Figure 6.** The charge–discharge profiles of Li-excess and conventional  $\text{LiFePO}_4$  (a), rate capabilities of the materials at different current densities (b) [99], and the comparison of electrochemical performance between “Li-rich” (c) and stoichiometric  $\text{LiFePO}_4$  (d) at different C-rates [9].

The “Li-rich” defects were found mainly in nanopowders of artificial cathode materials and have not been published for natural triphylite minerals. Although the investigation of monocrystalline  $\text{LiFePO}_4$  by means of single-crystal-neutron and X-ray diffraction confirms

the formation of an Li-excess material [101]. The monocrystals were produced by a flux growth technique, suggesting the possibility of off-stoichiometric defects occurring in nature.

Due to the structural similarity between triphylites and olivine silicates, the anionic sublattice experiences the same substitution tendencies. The phosphorus deficiency, which could also be assigned to the “off-stoichiometric” defect type, was observed in a natural ferrisicklerite with a suggested mechanism of substitution of phosphorus by hydroxyl groups [102]. First, the phosphorus deficiency in synthetic  $\text{LiFePO}_4$  was observed for highly defective material synthesized during short reaction times in [103]. As a result, the material encountered severe structural changes accompanying the  $\text{Li}^+$  de/insertion: a transition of  $\text{Fe}^{2+}$  and  $\text{Fe}^{3+}$  from the regular M2 position to M1. The material demonstrated poor electrochemical performance even at extremely low current densities of C/50 (Figure 7a). Despite the detailed structural changes, the phosphorus deficiency origin as well as the charge compensation mechanism were not revealed. The first attempt to precisely characterize the charge compensation mechanism of phosphorus-deficient triphylite cathodes or “hydrotriphylites” was made in [16]. Following the concept of water incorporation into olivine silicates, the phosphorus vacancy is supposed to be protonated with the formation of (OH) groups at the terminal oxygen atoms. The synthesis conditions leading to the production of phosphorus non-stoichiometry samples were found to be extremely diluted solutions of precursors. The defects were detected by FTIR spectroscopy and validated by joint synchrotron and neutron diffraction refinement. The influence of the hydroxyls on the material properties was observed as a drastic deterioration of the extracted specific capacity, with the possible explanation being significant structural changes [16]. The electrochemical performance of samples with different phosphorus deficiencies was investigated (Figure 7b). Increasing the hydroxyl defect concentration resulted in drastic deterioration of specific capacity of the material: 16% of phosphorus deficiency prevented  $\text{Li}^+$  from de/intercalation into the material structure [16].

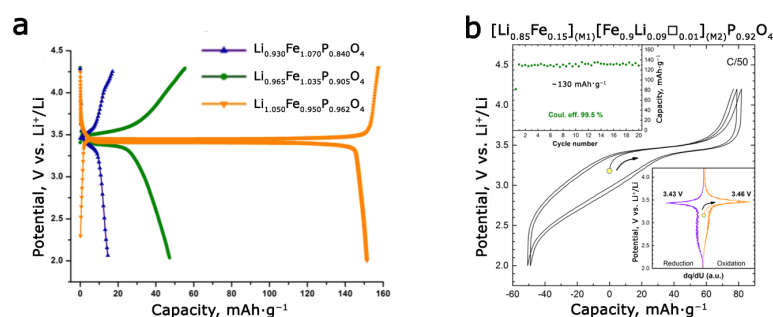


**Figure 7.** (a) The characterization of  $\text{LiFePO}_4$  containing 8% of P vacancies (the upper inset represents the cycling stability of the sample at C/50 rate, and the lower inset depicts the  $dQ/dV$  derivative [103]), and (b) the comparison of electrochemical performance of  $\text{LiFePO}_4$  materials with different P deficiency [16].

A further study conducted in [17] considered the Li–Fe–P–O<sub>2</sub> phase diagram constructed by means of first-principles calculations [104] and suggested the mechanism of charge compensation for P deficiency triphylite cathodes depending on oxygen chemical potential. Three different scenarios of hydrogen incorporation were taken into account: octahedrally coordinated Li or Fe vacancies, or phosphorus vacancy tetrahedral voids. It was found out that the minimum formation energy manifests the phosphorus vacancy compensation, while the substitution of Li or Fe vacancies is almost energetically equivalent.

The obtained computational results for triphylites are similar to those reported for olivine-type silicates long before, thus making the learning-from-nature concept a valuable tool for predicting and investigating the inner structure of the materials. Since the crystal structure defects influence the material properties significantly, the mineral genesis and formation conditions could be applied to the synthesis process of functional materials and could serve as additional ways of tuning the material properties. As a reference, the natural

genesis processes of dittmarite ( $\text{NH}_4\text{Fe}(\text{Mn})\text{PO}_4 \cdot \text{H}_2\text{O}$ ) and struvite ( $\text{NH}_4\text{MgPO}_4 \cdot \text{H}_2\text{O}$ ) minerals were studied from the thermodynamic point of view; as the result, the optimal conditions of precipitation were found [105]. Dittmarites are applied as precursors for triphylite  $\text{LiMPO}_4$  cathode synthesis [11,106]. Thus, the observed patterns could be applied to the optimization of the production process of the cathode materials.

#### 4. Discussion and Outlook

The mineral world is diverse and enormous; it hides a great number of hints and clues nurtured and validated by nature that are now at our disposal for application in the industry of functional materials. In the current review, we attempted to bind together the genesis and defect chemistry of olivine-group minerals with the synthesis processes and relationships between the defects and key properties of triphylite-type cathode materials. The tight connection between the minerals and cathodes made it possible to understand the main features of defect formation which led to the reduction of their negative impact on the electrochemical performance and production of defect-free materials as modern battery electrodes. A good example is hydroxyl defects for both natural silicate and phosphates of the triphylite family that were known among mineralogists since the mid-1970s but were observed only in the mid-2010s for synthetic  $\text{LiMPO}_4$  cathodes. Since the phosphate minerals are vulnerable to phosphorus non-stoichiometry especially during hydrothermal treatment, hydroxyl incorporation should be present in other functional phosphate-based materials besides those applied in batteries. Additional information that could be extracted from the mineral genesis is lattice distortion during cathode material cycling: the Jahn–Teller distortions that are responsible for low cycling stability of Mn-rich triphylite cathodes were described during the observation of triphylite–sicklerite–heterosite transformations by mineralogists long before the practical application of the corresponding electrode materials [67,107]. Moreover, the less effective diffusion of ions along the *b* crystallographic axis in the olivine-group silicates [45] was also observed well in advance of Li ion diffusion along the same axis in  $\text{LiMPO}_4$  cathodes.

The presence of antisite and hydroxyl defects impacts key material properties in a similar way: they deteriorate mechanical properties of olivine silicates and electrochemical performance of triphylite cathodes by the reason of inducing a charge imbalance in the crystal structure and reducing the rigidity of the  $\text{PO}_4$  framework. Thus, avoiding or minimizing defect formation becomes a top priority during material synthesis. On the other hand, the presence of the “Li-rich” defects that were found directly only in synthetic cathodes makes it possible to enhance the diffusion properties of the material with the sacrifice of the total capacity of the cathode. Another question is whether “Li-rich defects” are purely artificial or whether they might possibly be run across in natural minerals, since there is only one reference of additional Li ions present in the crystal structure of a synthetic  $\text{LiFePO}_4$  single crystal [101].

The same pattern of antisite defects formation is observed for  $\text{NaFePO}_4$ , although the defect formation is not the only problem of the material. Low  $\text{Na}^+$  diffusion coefficients and extremely high volume changes during  $\text{Na}^+$  de/insertion restrain the application of the material, despite the abundance of precursors and high theoretical capacity. An additional problem is that the maricite polymorph is more thermodynamically stable compared to its triphylite-structured counterpart, where the  $\text{NaO}_6$  octahedra are isolated in the crystal structure, so the activation energy for  $\text{Na}^+$  is high. In that sense, switching to fluoride phosphates ( $\text{Na}_2\text{FePO}_4\text{F}$ ) and mixed polyanion compositions ( $\text{Na}_2\text{Fe}(\text{C}_2\text{O}_4)(\text{HPO}_4)$ ) [108] seems to be a promising strategy in the way of mass production of high performance sodium-ion battery cathodes.

Additionally, other defects that occur in phosphate minerals could be engineered in the triphylite structure, for example, a partial substitution of  $\text{PO}_4^{3-}$  tetrahedra by  $\text{SiO}_4^{4-}$  with the possibility of additional Li ion insertion in the interstitial site. Considering that the ion size of  $\text{Si}^{4+}$  is larger than that of  $\text{P}^{5+}$ , such a type of substitution could be more favorable in materials with a bulkier *d* metal ion such as  $\text{Mn}^{2+}$ . Another case is Li inclusion

into the tetrahedral site that could be performed by an isomorphic substitution of  $\text{LiF}_4$  for  $\text{PO}_4$ . One more question that could be intriguing from the crystal chemistry point of view is whether it is possible to stabilize  $\text{LiFePO}_4$  in a maricite structure since there is a pronounced temperature dependence of phase coexistence between maricite and natrophylite in  $\text{NaFePO}_4$  [13] that can be expected in the case of  $\text{LiFePO}_4$  as well.

Overall, nature has already created the most suitable and energy-effective formation processes of most of the functional materials (or their predecessors) applied in modern industry. That information is usually contained in geochemical reports for natural ancestors of the materials—minerals. In that sense, a close collaboration among mineralogists, crystallographers and materials scientists is vital for ensuring effective breakthroughs in the manufacturing of modern functional materials.

**Author Contributions:** E.E.N.: writing—original draft preparation, writing—review and editing, visualization; D.A.A.: conceptualization, writing—review and editing; E.V.A.: writing—review and editing, funding acquisition, project administration; S.S.F.: conceptualization, writing—original draft preparation, writing—review and editing, visualization, supervision. All authors have read and agreed to the published version of the manuscript.

**Funding:** This research was funded by RSF, grant number 17-73-30006.

**Data Availability Statement:** Data sharing not applicable.

**Acknowledgments:** The authors are grateful to Aleksandra Savina, Ekaterina Marchenko and Polina Morozova for valuable discussions on the paper's contents.

**Conflicts of Interest:** The authors declare no conflict of interest.

## Appendix A

$(\text{Mg,Fe})_2\text{SiO}_4$	$\text{LiFePO}_4$	Description
$V_{Fe}''$	$V_{Fe}''$	Vacant Fe (M2) site
$V_{Mg}'$	$V_{Li}$	Vacant Mg/Li (M1) site
$V_{O}''$	$V_{O}''$	Vacant O site
$V_{Si}''$	$V_P$	Vacant Si/P site
$H_I$	$H_I$	A proton at an unoccupied interstitial position
$H'_{Mg}$	$H'_{Li}$	A proton in the Mg/Li site
$H'_{Fe}$	$H'_{Fe}$	A proton in the Fe site
$Mg_I''$	$Li_I$	$\text{Mg}^{2+}/\text{Li}^+$ at an unoccupied interstitial position
$Fe_I''$	$Fe_I''$	$\text{Fe}^{2+}$ at an unoccupied interstitial position
$O_I''$	$O_I''$	$\text{O}^{2-}$ at an unoccupied interstitial position
$Si_I''''$	$P_I''''$	$\text{Si}^{4+}$ at an unoccupied interstitial position
$e'$	$e'$	Electron in the conduction band
$h'$	$h'$	Hole in the valence band
$Fe_{Mg}''$	$Fe_{Li}''$	$\text{Fe}^{3+}$ in the Mg/Li (M1) site (antisite defect)
$Fe_{Fe}''$	$Fe_{Fe}''$	$\text{Fe}^{3+}$ in the Fe (M2) site (Fe oxidation)
$Mg_{Mg}^\times$	$Li_{Li}^\times$	$\text{Mg}^{2+}/\text{Li}^+$ ion in the Mg/Li site
$Fe_{Mg}^\times$	$Fe_{Li}''$	$\text{Fe}^{2+}$ ion in the Mg/Li site (antisite defect)
$Fe_{Fe}^\times$	$Fe_{Fe}^\times$	$\text{Fe}^{2+}$ ion in the Fe site
$Si_{Si}^\times$	$P_P^\times$	$\text{Si}^{4+}/\text{P}^{5+}$ ion in the Si/P site
$O_o^\times$	$O_o^\times$	$\text{O}^{2-}$ ion in the O site

## References

1. Berry, A.J.; Hermann, J.; O'Neill, H.S.C.; Foran, G.J. Fingerprinting the Water Site in Mantle Olivine. *Geology* **2005**, *33*, 869. [CrossRef]
2. The Effect of Water on the Electrical Conductivity of Olivine | Nature. Available online: <https://www.nature.com/articles/nature05256> (accessed on 28 March 2023).
3. Water in Earth's Mantle: The Role of Nominally Anhydrous Minerals | Science. Available online: <https://www.science.org/doi/10.1126/science.255.5050.1391> (accessed on 28 March 2023).
4. Padhi, A.K.; Nanjundaswamy, K.S.; Goodenough, J.B. Phospho-olivines as Positive-Electrode Materials for Rechargeable Lithium Batteries. *J. Electrochem. Soc.* **1997**, *144*, 1188. [CrossRef]
5. Zhang, S.S. Problems and Their Origins of Ni-Rich Layered Oxide Cathode Materials. *Energy Storage Mater.* **2020**, *24*, 247–254. [CrossRef]
6. Julien, C.M.; Mauger, A.; Zaghib, K.; Groult, H. Comparative Issues of Cathode Materials for Li-Ion Batteries. *Inorganics* **2014**, *2*, 132–154. [CrossRef]
7. Nazarov, E.E.; Dembitskiy, A.D.; Trussov, I.A.; Tyablikov, O.A.; Glazkova, I.S.; Alexey, S.V.; Presniakov, I.A.; Mikheev, I.V.; Morozov, A.V.; Nikitina, V.A.; et al. A Li-Rich Strategy towards Advanced Mn-Doped Triphylite Cathodes for Li-Ion Batteries. *Energy Adv.* **2023**, *2*, 328–337. [CrossRef]
8. Nazarov, E.E.; Tyablikov, O.A.; Nikitina, V.A.; Antipov, E.V.; Fedotov, S.S. Polyacrylonitrile-Derived Carbon Nanocoating for Long-Life High-Power Phosphate Electrodes. *Appl. Nano* **2023**, *4*, 25–37. [CrossRef]
9. Drozhzhin, O.A.; Sobolev, A.V.; Sumanov, V.D.; Glazkova, I.S.; Aksyonov, D.A.; Grebenshchikova, A.D.; Tyablikov, O.A.; Alekseeva, A.M.; Mikheev, I.V.; Dovgaliuk, I.; et al. Exploring the Origin of the Superior Electrochemical Performance of Hydrothermally Prepared Li-Rich Lithium Iron Phosphate  $\text{Li}_{1+\delta}\text{Fe}_{1-\delta}\text{PO}_4$ . *J. Phys. Chem. C* **2020**, *124*, 126–134. [CrossRef]
10. Ravnsbæk, D.B.; Xiang, K.; Xing, W.; Borkiewicz, O.J.; Wiaderek, K.M.; Gionet, P.; Chapman, K.W.; Chupas, P.J.; Chiang, Y.-M. Extended Solid Solutions and Coherent Transformations in Nanoscale Olivine Cathodes. *Nano Lett.* **2014**, *14*, 1484–1491. [CrossRef]
11. Koleva, V.G.; Boyadzhieva, T.J.; Stoyanova, R.K. Crystal and Morphology Design of Dittmarite-Type Ammonium Iron–Manganese Phosphates,  $\text{NH}_4\text{Mn}_{1-x}\text{FexPO}_4 \cdot \text{H}_2\text{O}$ , as Precursors for Phospho-Olivine Electrodes. *Cryst. Growth Des.* **2019**, *19*, 3744–3754. [CrossRef]
12. Freeze Drying under Vacuum Assisted Synthesis of  $\text{LiFePO}_4$ @MWCNTs Composite with Phytic Acid as Phosphorus Source for Advanced Li-Storage-Science Direct. Available online: <https://www.sciencedirect.com/science/article/abs/pii/S0042207X21004905> (accessed on 28 April 2023).
13. Vignola, P.; Hatert, F.; Fransolet, A.-M.; Medenbach, O.; Diella, V.; Andò, S. Karenwebberite,  $\text{Na}(\text{Fe}^{2+}, \text{Mn}^{2+})\text{PO}_4$ , a New Member of the Triphylite Group from the Malpensata Pegmatite, Lecco Province, Italy. *Am. Mineral.* **2013**, *98*, 767–772. [CrossRef]
14. Heubner, C.; Heiden, S.; Schneider, M.; Michaelis, A. In-Situ Preparation and Electrochemical Characterization of Submicron Sized  $\text{NaFePO}_4$  Cathode Material for Sodium-Ion Batteries. *Electrochim. Acta* **2017**, *233*, 78–84. [CrossRef]
15. Zhu, Y.; Xu, Y.; Liu, Y.; Luo, C.; Wang, C. Comparison of Electrochemical Performances of Olivine  $\text{NaFePO}_4$  in Sodium-Ion Batteries and Olivine  $\text{LiFePO}_4$  in Lithium-Ion Batteries. *Nanoscale* **2012**, *5*, 780–787. [CrossRef] [PubMed]
16. Sumanov, V.D.; Aksyonov, D.A.; Drozhzhin, O.A.; Presniakov, I.; Sobolev, A.V.; Glazkova, I.; Tsirlin, A.A.; Rupasov, D.; Senyshyn, A.; Kolesnik, I.V.; et al. “Hydrotriphylites”  $\text{Li}_{1-x}\text{Fe}_{1+x}(\text{PO}_4)_{1-y}(\text{OH})_{4y}$  as Cathode Materials for Li-Ion Batteries. *Chem. Mater.* **2019**, *31*, 5035–5046. [CrossRef]
17. Aksyonov, D.A.; Varlamova, I.; Trussov, I.A.; Savina, A.A.; Senyshyn, A.; Stevenson, K.J.; Abakumov, A.M.; Zhugayevych, A.; Fedotov, S.S. Hydroxyl Defects in  $\text{LiFePO}_4$  Cathode Material: DFT+ *U* and an Experimental Study. *Inorg. Chem.* **2021**, *60*, 5497–5506. [CrossRef] [PubMed]
18. Burns, R.G. Site Preferences of Transition Metal Ions in Silicate Crystal Structures. *Chem. Geol.* **1970**, *5*, 275–283. [CrossRef]
19. Brrle, J.D. Crystal structures of natural olivines. *Am. Mineral.* **1968**, *53*, 807–824.
20. Aikawa, N.; Tokonami, M. Crystal Structure and Cation Distribution of “Cleavable” Olivines. *Mineral. J.* **1987**, *13*, 271–279. [CrossRef]
21. Avdeev, M.; Mohamed, Z.; Ling, C.D.; Lu, J.; Tamaru, M.; Yamada, A.; Barpanda, P. Magnetic Structures of  $\text{NaFePO}_4$  Maricite and Triphylite Polymorphs for Sodium-Ion Batteries. *Inorg. Chem.* **2013**, *52*, 8685–8693. [CrossRef]
22. Stewart, D.B. Petrogenesis of Lithium-Rich Pegmatites. *Am. Mineral.* **1978**, *63*, 970–980.
23. The Classification of Granitic Pegmatites Revisited | The Canadian Mineralogist | GeoScienceWorld. Available online: <https://pubs.geoscienceworld.org/canmin/article-abstract/43/6/2005/126681/THE-CLASSIFICATION-OF-GRANITIC-PEGMATITES?redirectedFrom=fulltext> (accessed on 28 March 2023).
24. Li, Z.; Shinno, I. Next Nearest Neighbor Effects in Triphylite and Related Phosphate Minerals. *Mineral. J.* **1997**, *19*, 99–107. [CrossRef]
25. The Crystal Structure of the New Mineral Maricite,  $\text{NaFePO}_4$  | Semantic Scholar. Available online: <https://www.semanticscholar.org/paper/The-crystal-structure-of-the-new-mineral-maricite%2C-Page-Donnay/a440fc91063a0b9e8c0be502df61aef8c592076a> (accessed on 28 March 2023).
26. The Crystal Structure of  $\text{NaMnPO}_4$  | Semantic Scholar. Available online: <https://www.semanticscholar.org/paper/The-crystal-structure-of-NaMnPO4-Moring-Kostiner/7b749288d2fce21372458ad07dba97d9389813dd> (accessed on 28 March 2023).

27. Rouse, G.; Rodriguez-Carvajal, J.; Patoux, S.; Masquelier, C. Magnetic Structures of the Triphylite  $\text{LiFePO}_4$  and of Its Delithiated Form  $\text{FePO}_4$ . *Chem. Mater.* **2003**, *15*, 4082–4090. [[CrossRef](#)]
28. Topochemical Synthesis of Sodium Metal Phosphate Olivines for Sodium-Ion Batteries | Chemistry of Materials. Available online: <https://pubs.acs.org/doi/10.1021/cm200450y> (accessed on 28 March 2023).
29. Storage Performance of  $\text{Mg}^{+++}$  Substituted  $\text{NaMnPO}_4$  with an Olivine Structure-RSC Advances (RSC Publishing). Available online: <https://pubs.rsc.org/en/content/articlelanding/2020/ra/d0ra05698g> (accessed on 20 May 2023).
30. Precursor-Based Methods for Low-Temperature Synthesis of Defectless  $\text{NaMnPO}_4$  with an Olivine- and Maricite-Type Structure-CrystEngComm (RSC Publishing). Available online: <https://pubs.rsc.org/en/content/articlelanding/2013/ce/c3ce41545g> (accessed on 20 May 2023).
31. Denisov, I.P.; Yakovlev, V.Y. Formation of Self-Trapped Exitons and Defects in Alkali Halides under Pulsed Electron Irradiation. *Izv. Akad. Nauk. Latv. SSR Seriya Fiz. I Tekhnicheskikh Nauk.* **1990**, *3*, 66–72.
32. H-Center and V-Center Defects in Hybrid Halide Perovskites | ACS Energy Letters. Available online: <https://pubs.acs.org/doi/full/10.1021/acseenergylett.7b00995> (accessed on 28 March 2023).
33. Chen, W.; Tegenkamp, C.; Pfnür, H.; Bredow, T. Color Centers in NaCl by Hybrid Functionals. *Phys. Rev. B* **2010**, *82*, 104106. [[CrossRef](#)]
34. Gordon, R.B.; Nowick, A.S. Structure Sensitivity of the X-ray Coloration of NaCl Crystals. *Phys. Rev.* **1956**, *101*, 977–983. [[CrossRef](#)]
35. Polanco, C.A.; Lindsay, L. Thermal Conductivity of InN with Point Defects from First Principles. *Phys. Rev. B* **2018**, *98*, 014306. [[CrossRef](#)]
36. Stern, R.; Wang, T.; Carrete, J.; Mingo, N.; Madsen, G.K.H. Influence of Point Defects on the Thermal Conductivity in FeSi. *Phys. Rev. B* **2018**, *97*, 195201. [[CrossRef](#)]
37. Rissouli, K.; Benkhoucha, K.; Ramos-Barrado, J.R.; Julien, C. Electrical Conductivity in Lithium Orthophosphates. *Mater. Sci. Eng. B* **2003**, *98*, 185–189. [[CrossRef](#)]
38. Reznik, A.; Uzan-Saguy, C.; Kalish, R. Effects of Point Defects on the Electrical Properties of Doped Diamond. *Diam. Relat. Mater.* **2000**, *9*, 1051–1056. [[CrossRef](#)]
39. Hong, J.; Wang, C.S.; Chen, X.; Upreti, S.; Whittingham, M.S. Vanadium Modified  $\text{LiFePO}_4$  Cathode for Li-Ion Batteries. *Electrochem. Solid-State Lett.* **2008**, *12*, A33. [[CrossRef](#)]
40. Maier, J.; Amin, R. Defect Chemistry of  $\text{LiFePO}_4$ . *J. Electrochem. Soc.* **2008**, *155*, A339. [[CrossRef](#)]
41. Walker, A.M.; Woodley, S.M.; Slater, B.; Wright, K. A Computational Study of Magnesium Point Defects and Diffusion in Forsterite. *Phys. Earth Planet. Inter.* **2009**, *172*, 20–27. [[CrossRef](#)]
42. Kröger, F.A.; Vink, H.J. Relations between the Concentrations of Imperfections in Crystalline Solids. In *Solid State Physics*; Seitz, F., Turnbull, D., Eds.; Academic Press: Cambridge, MA, USA, 1956; Volume 3, pp. 307–435.
43. Zhang, B. An Overview of Fe–Mg Interdiffusion in Mantle Minerals. *Surv. Geophys.* **2017**, *38*, 727–755. [[CrossRef](#)]
44. Ghose, S.; Wan, C. Strong site preference of  $\text{Co}^{2+}$  in olivine,  $\text{Co}_{1.10}\text{Mg}_{0.90}\text{SiO}_4$ . *Contrib. Miner. Pet.* **1974**, *47*, 131–140. [[CrossRef](#)]
45. Buening, D.K.; Buseck, P.R. Fe–Mg lattice diffusion in olivine. *J. Geophys. Res. Atmos.* **1973**, *78*, 6852–6862. [[CrossRef](#)]
46. Misener, D.J. *Cation Diffusion in Olivine to 1400 °C and 35 KB*; The University of British Columbia: Kelowna, BC, USA, 1973.
47. Chakraborty, S.; Knoche, R.; Schulze, H.; Rubie, D.C.; Dobson, D.; Ross, N.L.; Angel, R.J. Enhancement of Cation Diffusion Rates Across the 410-Kilometer Discontinuity in Earth’s Mantle. *Science* **1999**, *283*, 362–365. [[CrossRef](#)]
48. Jaoul, O.; Bertran-Alvarez, Y.; Liebermann, R.C.; Price, G.D. Fe, Mg interdiffusion in olivine up to 9 GPa at  $T = 600\text{--}900\text{ °C}$ ; experimental data and comparison with defect calculations. *Phys. Earth Planet. Inter.* **1995**, *89*, 199–218. [[CrossRef](#)]
49. Dohmen, R.; Chakraborty, S. Fe–Mg Diffusion in Olivine II: Point Defect Chemistry, Change of Diffusion Mechanisms and a Model for Calculation of Diffusion Coefficients in Natural Olivine. *Phys Chem Miner.* **2007**, *34*, 409–430. [[CrossRef](#)]
50. Tachibana, S.; Tamada, S.; Kawasaki, H.; Ozawa, K.; Nagahara, H. Interdiffusion of Mg–Fe in Olivine at 1400–1600 °C and 1 Atm Total Pressure. *Phys. Chem. Miner.* **2013**, *40*, 511–519. [[CrossRef](#)]
51. Chakraborty, S. Diffusion Coefficients in Olivine, Wadsleyite and Ringwoodite. *Rev. Mineral. Geochem.* **2010**, *72*, 603–639. [[CrossRef](#)]
52. Chatterjee, S.; Sengupta, S.; Saha-Dasgupta, T.; Chatterjee, K.; Mandal, N. Site Preference of Fe Atoms in  $\text{FeMgSiO}_4$  and  $\text{FeMg}(\text{SiO}_3)_2$  Studied by Density Functional Calculations. *Phys. Rev. B* **2009**, *79*, 115103. [[CrossRef](#)]
53. Redfern, S.A.T.; Artioli, G.; Rinaldi, R.; Henderson, C.M.B.; Knight, K.S.; Wood, B.J. Octahedral cation ordering in olivine at high temperature. II: An in situ neutron powder diffraction study on synthetic  $\text{MgFeSiO}_4$  (Fa50). *Phys. Chem. Miner.* **2000**, *27*, 630–637. [[CrossRef](#)]
54. Kolesov, B.A.; Geiger, C.A. A Raman spectroscopic study of Fe–Mg olivines. *Phys. Chem. Miner.* **2004**, *31*, 142–154. [[CrossRef](#)]
55. Das, P.K.; Mandal, N.; Arya, A. Effects of cation ordering on the elastic and electronic properties of Mg–Fe silicate phases at high pressures. *J. Appl. Phys.* **2017**, *122*, 225107. [[CrossRef](#)]
56. Mei, S.; Kohlstedt, D.L. Influence of water on plastic deformation of olivine aggregates: 1. Diffusion creep regime. *J. Geophys. Res. Solid Earth* **2000**, *105*, 21457–21469. [[CrossRef](#)]
57. Walker, A.M.; Hermann, J.; Berry, A.J.; O’Neill, H.S.C. Three Water Sites in Upper Mantle Olivine and the Role of Titanium in the Water Weakening Mechanism. *J. Geophys. Res.* **2007**, *112*, B05211. [[CrossRef](#)]

58. Balan, E.; Ingrin, J.; Delattre, S.; Kovács, I.; Blanchard, M. Theoretical infrared spectrum of OH-defects in forsterite. *Eur. J. Miner.* **2011**, *23*, 285–292. [CrossRef]
59. Churakov, S.V.; Khisina, N.R.; Urusov, V.S.; Wirth, R. First-Principles Study of  $(\text{MgH}_2\text{SiO}_4)_n(\text{Mg}_2\text{SiO}_4)$  Hydrated Olivine Structures. I. Crystal Structure Modelling of Hydrated Olivine Hy-2a  $(\text{MgH}_2\text{SiO}_4) \bullet 3(\text{Mg}_2\text{SiO}_4)$ . *Phys. Chem. Miner.* **2003**, *30*, 1–11. [CrossRef]
60. Blanchard, M.; Ingrin, J.; Balan, E.; Kovács, I.; Withers, A.C. Effect of Iron and Trivalent Cations on OH Defects in Olivine. *Am. Mineral.* **2017**, *102*, 302–311. [CrossRef]
61. McGetchin, T.R.; Silver, L.T.; Chodos, A.A. Titanoclinohumite: A Possible Mineralogical Site for Water in the Upper Mantle. *J. Geophys. Res.* **1970**, *75*, 255–259. [CrossRef]
62. Kohlstedt, D.L.; Mackwell, S.J. Diffusion of Hydrogen and Intrinsic Point Defects in Olivine. *Z. Für Phys. Chem.* **1998**, *207*, 147–162. [CrossRef]
63. Schock, R.N.; Duba, A.G. Point Defects and the Mechanisms of Electrical Conduction in Olivine. *Point Defects Miner.* **2013**, *31*, 88–96. [CrossRef]
64. Defects in Solids | Wiley. Available online: <https://www.wiley.com/en-us/Defects+in+Solids-p-9780470380734> (accessed on 28 March 2023).
65. Kramer, M.J.; Mendeleev, M.I.; Napolitano, R.E. In Situ Observation of Antisite Defect Formation during Crystal Growth. *Phys. Rev. Lett.* **2010**, *105*, 245501. [CrossRef] [PubMed]
66. Fehr, K.T.; Hochleitner, R.; Schmidbauer, E.; Schneider, J. Mineralogy, Mössbauer Spectra and Electrical Conductivity of Triphylite  $\text{Li}(\text{Fe}^{2+}, \text{Mn}^{2+})\text{PO}_4$ . *Phys. Chem. Miner.* **2007**, *34*, 485–494. [CrossRef]
67. Hatert, F.; Ottolini, L.; Wouters, J.; Fontan, F. A Structural Study of the Lithiophilite-Sicklerite Series. *Can. Mineral.* **2012**, *50*, 843–854. [CrossRef]
68. Drozhzhin, O.A.; Tereshchenko, I.V.; Emerich, H.; Antipov, E.V.; Abakumov, A.M.; Chernyshov, D. An Electrochemical Cell with Sapphire Windows for Operando Synchrotron X-ray Powder Diffraction and Spectroscopy Studies of High-Power and High-Voltage Electrodes for Metal-Ion Batteries. *J. Synchrotron. Radiat.* **2018**, *25*, 468–472. [CrossRef] [PubMed]
69. Islam, M.S.; Driscoll, D.J.; Fisher, C.A.J.; Slater, P.R. Atomic-Scale Investigation of Defects, Dopants, and Lithium Transport in the  $\text{LiFePO}_4$  Olivine-Type Battery Material. *Chem. Mater.* **2005**, *17*, 5085–5092. [CrossRef]
70. Fisher, C.A.J.; Prieto, V.M.H.; Islam, M.S. Lithium Battery Materials  $\text{LiMPO}_4$  (M = Mn, Fe, Co, and Ni): Insights into Defect Association, Transport Mechanisms, and Doping Behavior. Available online: <https://pubs.acs.org/doi/full/10.1021/cm801262x> (accessed on 30 May 2023).
71. Malik, R.; Burch, D.; Bazant, M.; Ceder, G. Particle Size Dependence of the Ionic Diffusivity. Available online: <https://pubs.acs.org/doi/full/10.1021/nl1023595> (accessed on 30 May 2023).
72. Tripathi, R.; Wood, S.M.; Islam, M.S.; Nazar, L.F. Na-Ion Mobility in Layered  $\text{Na}_2\text{FePO}_4\text{F}$  and Olivine  $\text{Na}[\text{Fe}, \text{Mn}]\text{PO}_4$ . *Energy Environ. Sci.* **2013**, *6*, 2257–2264. [CrossRef]
73. Galceran, M.; Roddatis, V.; Zúñiga, F.J.; Pérez-Mato, J.M.; Acebedo, B.; Arenal, R.; Peral, I.; Rojo, T.; Casas-Cabanas, M. Na-Vacancy and Charge Ordering in  $\text{Na}_{\approx 2/3}\text{FePO}_4$ . *Chem. Mater.* **2014**, *26*, 3289–3294. [CrossRef]
74. Casas-Cabanas, M.; Roddatis, V.V.; Saurel, D.; Kubiak, P.; Carretero-González, J.; Palomares, V.; Serras, P.; Rojo, T. Crystal Chemistry of Na Insertion/Deinsertion in  $\text{FePO}_4$ - $\text{NaFePO}_4$ . *J. Mater. Chem.* **2012**, *22*, 17421–17423. [CrossRef]
75. Lee, J.; Zhou, W.; Idrobo, J.C.; Pennycook, S.J.; Pantelides, S.T. Vacancy-Driven Anisotropic Defect Distribution in the Battery-Cathode Material  $\text{LiFePO}_4$ . *Phys. Rev. Lett.* **2011**, *107*, 085507. [CrossRef]
76. Kuss, C.; Liang, G.; Schougaard, S.B. Atomistic Modeling of Site Exchange Defects in Lithium Iron Phosphate and Iron Phosphate. *J. Mater. Chem.* **2012**, *22*, 24889–24893. [CrossRef]
77. Wang, J.; Sun, X. Olivine  $\text{LiFePO}_4$ : The Remaining Challenges for Future Energy Storage. *Energy Environ. Sci.* **2015**, *8*, 1110–1138. [CrossRef]
78. Hydrothermal Synthesis of Lithium Iron Phosphate Cathodes. *Electrochem. Commun.* **2001**, *3*, 505–508. [CrossRef]
79. Cho, M.-Y.; Kim, K.-B.; Lee, J.-W.; Kim, H.; Kim, H.; Kang, K.; Roh, K.C. Defect-Free Solvothermally Assisted Synthesis of Microspherical Mesoporous  $\text{LiFePO}_4/\text{C}$ . *RSC Adv.* **2013**, *3*, 3421–3427. [CrossRef]
80. Yang, S.; Song, Y.; Zavalij, P.Y.; Stanley Whittingham, M. Reactivity, Stability and Electrochemical Behavior of Lithium Iron Phosphates. *Electrochem. Commun.* **2002**, *4*, 239–244. [CrossRef]
81. Chen, J.; Vacchio, M.J.; Wang, S.; Chernova, N.; Zavalij, P.Y.; Whittingham, M.S. The Hydrothermal Synthesis and Characterization of Olivines and Related Compounds for Electrochemical Applications. *Solid State Ion.* **2008**, *178*, 1676–1693. [CrossRef]
82. Park, K.-Y.; Park, I.; Kim, H.; Lim, H.; Hong, J.; Kim, J.; Kang, K. Anti-Site Reordering in  $\text{LiFePO}_4$ : Defect Annihilation on Charge Carrier Injection. Available online: <https://pubs.acs.org/doi/full/10.1021/cm502432q> (accessed on 30 May 2023).
83. Chen, J.; Graetz, J. Study of Antisite Defects in Hydrothermally Prepared  $\text{LiFePO}_4$  by in Situ X-ray Diffraction. Available online: <https://pubs.acs.org/doi/full/10.1021/am200141a> (accessed on 30 May 2023).
84. Gibot, P.; Casas-Cabanas, M.; Laffont, L.; Lévassieur, S.; Carlach, P.; Hamelet, S.; Tarascon, J.-M.; Masquelier, C. Room-Temperature Single-Phase Li Insertion/Extraction in Nanoscale  $\text{Li}_x\text{FePO}_4$ . *Nat. Mater.* **2008**, *7*, 741–747. [CrossRef]
85. Yamada, A.; Koizumi, H.; Sonoyama, N.; Kanno, R. Phase Change in  $\text{Li}_x\text{FePO}_4$ . *Electrochem. Solid-State Lett.* **2005**, *8*, A409. [CrossRef]

86. Delacourt, C.; Poizot, P.; Levasseur, S.; Masquelier, C. Size Effects on Carbon-Free LiFePO<sub>4</sub> Powders: The Key to Superior Energy Density. *Electrochem. Solid-State Lett.* **2006**, *9*, A352. [[CrossRef](#)]
87. Zhao, Y.; Peng, L.; Liu, B.; Yu, G. Single-Crystalline LiFePO<sub>4</sub> Nanosheets for High-Rate Li-Ion Batteries. Available online: <https://pubs.acs.org/doi/full/10.1021/nl5008568> (accessed on 30 May 2023).
88. Liang, Y.; Wen, K.; Mao, Y.; Liu, Z.; Zhu, G.; Yang, F.; He, W. Shape and Size Control of LiFePO<sub>4</sub> for High-Performance Lithium-Ion Batteries. *ChemElectroChem* **2015**, *2*, 1227–1237. [[CrossRef](#)]
89. Paoletta, A.; Turner, S.; Bertoni, G.; Hovington, P.; Flacau, R.; Boyer, C.; Feng, Z.; Colombo, M.; Marras, S.; Prato, M.; et al. Accelerated Removal of Fe-Antisite Defects while Nanosizing Hydrothermal LiFePO<sub>4</sub> with Ca<sup>2+</sup>. Available online: <https://pubs.acs.org/doi/full/10.1021/acs.nanolett.6b00334> (accessed on 30 May 2023).
90. Zou, Y.; Chang, G.; Chen, S.; Liu, T.; Xia, Y.; Chen, C.; Yang, D. Alginate/r-GO Assisted Synthesis of Ultrathin LiFePO<sub>4</sub> Nanosheets with Oriented (0 1 0) Facet and Ultralow Antisite Defect. *Chem. Eng. J.* **2018**, *351*, 340–347. [[CrossRef](#)]
91. Drozhzhin, O.A.; Sumanov, V.D.; Karakulina, O.M.; Abakumov, A.M.; Hadermann, J.; Baranov, A.N.; Stevenson, K.J.; Antipov, E.V. Switching between Solid Solution and Two-Phase Regimes in the Li<sub>1-x</sub>Fe<sub>1-y</sub>MnyPO<sub>4</sub> Cathode Materials during Lithium (de)Insertion: Combined PITT, in Situ XRPD and Electron Diffraction Tomography Study. *Electrochim. Acta* **2016**, *191*, 149–157. [[CrossRef](#)]
92. Chung, S.-Y.; Choi, S.-Y.; Yamamoto, T.; Ikuhara, Y. Orientation-Dependent Arrangement of Antisite Defects in Lithium Iron(II) Phosphate Crystals. *Angew. Chem. Int. Ed.* **2009**, *48*, 543–546. [[CrossRef](#)] [[PubMed](#)]
93. Chung, S.-Y.; Choi, S.-Y.; Yamamoto, T.; Ikuhara, Y. Atomic-Scale Visualization of Antisite Defects in LiFePO<sub>4</sub>. *Phys. Rev. Lett.* **2008**, *100*, 125502. [[CrossRef](#)]
94. Chapman, C.A. Large Magnesia-Rich Triphylite Crystals in Pegmatite. *Am. Mineral.* **1943**, *28*, 90–98.
95. Tealdi, C.; Spreafico, C.; Mustarelli, P. Lithium Diffusion in Li<sub>1-x</sub>FePO<sub>4</sub>: The Effect of Cationic Disorder. *J. Mater. Chem.* **2012**, *22*, 24870–24876. [[CrossRef](#)]
96. Boulfelfel, S.E.; Seifert, G.; Leoni, S. Atomistic Investigation of Li<sup>+</sup> Diffusion Pathways in the Olivine LiFePO<sub>4</sub> Cathode Material. *J. Mater. Chem.* **2011**, *21*, 16365–16372. [[CrossRef](#)]
97. Chung, S.-Y.; Choi, S.-Y.; Lee, S.; Ikuhara, Y. Distinct Configurations of Antisite Defects in Ordered Metal Phosphates: Comparison between LiMnPO<sub>4</sub> and LiFePO<sub>4</sub>. *Phys. Rev. Lett.* **2012**, *108*, 195501. [[CrossRef](#)]
98. Francis, C.A. The Forsterite-Tephroite Series: I Crystal Structure Refinements. Available online: <https://www.semanticscholar.org/paper/The-forsterite-tephroite-series-%3A-I.-Crystal-FReNcIs/b6c28c0f2f8accb9386cdf33ff498a28584362a0> (accessed on 30 May 2023).
99. Park, K.-Y.; Park, I.; Kim, H.; Yoon, G.; Gwon, H.; Cho, Y.; SooYun, Y.; Kim, J.-J.; Lee, S.; Ahn, D.; et al. Lithium-Excess Olivine Electrode for Lithium Rechargeable Batteries. *Energy Environ. Sci.* **2016**, *9*, 2902–2915. [[CrossRef](#)]
100. Zeng, H.; Gu, Y.; Teng, G.; Liu, Y.; Zheng, J.; Pan, F. Ab Initio Identification of the Li-Rich Phase in LiFePO<sub>4</sub>. *Phys. Chem. Chem. Phys.* **2018**, *20*, 17497–17503. [[CrossRef](#)]
101. Janssen, Y.; Santhanagopalan, D.; Qian, D.; Chi, M.; Wang, X.; Hoffmann, C.; Meng, Y.S.; Khalifah, P.G. Reciprocal Salt Flux Growth of LiFePO<sub>4</sub> Single Crystals with Controlled Defect Concentrations. *Chem. Mater.* **2013**, *25*, 4574–4584. [[CrossRef](#)]
102. Albertia, A. The Crystal Structure of Ferrisicklerite, Li<sub>1-x</sub>(Fe<sup>3+</sup>, Mn<sup>2+</sup>)PO<sub>4</sub>. *Acta. Cryst. B* **1976**, *32*, 2761–2764. [[CrossRef](#)]
103. Amisse, R.; Sougrati, M.T.; Stievano, L.; Davoisne, C.; Dražič, G.; Budič, B.; Dominko, R.; Masquelier, C. Singular Structural and Electrochemical Properties in Highly Defective LiFePO<sub>4</sub> Powders. *Chem. Mater.* **2015**, *27*, 4261–4273. [[CrossRef](#)]
104. Ong, S.P.; Wang, L.; Kang, B.; Ceder, G. Li–Fe–P–O<sub>2</sub> Phase Diagram from First Principles Calculations. *Chem. Mater.* **2008**, *20*, 1798–1807. [[CrossRef](#)]
105. Asmare, A. Brodie Whitehead Thermodynamic Principles of Dittmarite Precipitation. *JESE-B* **2018**, *7*, 331–336. [[CrossRef](#)]
106. Koleva, V.; Stoyanova, R.; Zhecheva, E.; Nihtianova, D. Dittmarite Precursors for Structure and Morphology Directed Synthesis of Lithium Manganese Phospho-Olivine Nanostructures. *CrystEngComm* **2014**, *16*, 7515–7524. [[CrossRef](#)]
107. Eventoff, W.; Martin, R.; Peacor, D.R. The Crystal Structure of Heterosite1. *Am. Mineral.* **1972**, *57*, 45–51.
108. Pramanik, A.; Bradford, A.J.; Lee, S.L.; Lightfoot, P.; Armstrong, A.R. Na<sub>2</sub>Fe(C<sub>2</sub>O<sub>4</sub>)(HPO<sub>4</sub>): A Promising New Oxalate-Phosphate Based Mixed Polyanionic Cathode for Li/Na Ion Batteries. *J. Phys. Mater.* **2021**, *4*, 024004. [[CrossRef](#)]

**Disclaimer/Publisher’s Note:** The statements, opinions and data contained in all publications are solely those of the individual author(s) and contributor(s) and not of MDPI and/or the editor(s). MDPI and/or the editor(s) disclaim responsibility for any injury to people or property resulting from any ideas, methods, instructions or products referred to in the content.